The scaffold protein PRR14L links the PP2A-TACC3 axis to mitotic fidelity and sensitivity to MPS1 inhibition

Albert Z. Liu[1,2], Akshay Narkar[1], Keming Li[2], Thierry Bertomeu[3], Blake A. Johnson[1], Jasmin Coulombe-Huntington[4], Yi Dong[1], Jin Zhu[2], Mike Tyers[5,6], Rong Li[1,2,7]

1. Department of Cell Biology, Johns Hopkins School of Medicine, Baltimore, MD 21205, USA
2. Mechanobiology Institute, National University of Singapore, Singapore 117411, Singapore
3. The ChemoGenix CRISPR screening facility of the Institute for Research in Immunology and Cancer, University of Montreal, 2950 Chemin de Polytechnique, Montréal, QC H3T 1J4, Canada
4. Department of Bioengineering, McGill University, Montreal, QC H3A 0E9, Canada
5. Department of Molecular Genetics, University of Toronto; Toronto, Ontario M5S 1A8, Canada
6. Program in Molecular Medicine, Peter Gilgan Centre for Research and Learning, The Hospital for Sick Children, Toronto, ON M5G 0A4, Canada
7. Department of Biological Sciences, National University of Singapore, Singapore 117558, Singapore

*Correspondence and lead contact: Rong Li (mbihead@nus.edu.sg)

Abstract

Aneuploidy is a hallmark of cancer and is a potential vulnerability that can be selectively targeted. To systematically identify genes that affect the incidence and fitness of aneuploid cells, we conducted a genome-wide CRISPR/Cas9 screen using NMS-P715, an inhibitor of the spindle assembly checkpoint (SAC) kinase Mps1/TTK. In this study, we identified a number of genes known to regulate aneuploidy and mitosis, and subsequently focused on *PRR14L*, a ubiquitously expressed gene previously implicated in chronic myelomonocytic leukemia (CMML). Proximity labeling of PRR14L using TurboID revealed several cell division proteins, including the PP2A-B56 phosphatase complex and the spindle assembly factor TACC3, as PRR14L-interacting proteins. Loss of PRR14L prolongs SAC-dependent mitotic arrest in response to microtubule depolymerization but, paradoxically, leads to catastrophic mitotic errors upon SAC abrogation by MPS1 inhibitors. A model derived from our findings provides a rationale for exploiting MPS1 inhibition as a potential vulnerability in cancers containing either PRR14L loss of function mutations or FGFR-TACC3 fusions.

Introduction

Intratumor heterogeneity, drug resistance, and metastasis constitute major challenges in cancer therapy. All these have been associated with aneuploidy, a cellular state whereby the chromosome number is not a multiple of the haploid set. Aneuploidy in cancer is a consequence of chromosomal instability (CIN) due to heightened frequency of chromosome mis-segregation (Bakhoum and Landau, 2017; Bakhoum *et al.*, 2018; Replogle *et al.*, 2020). The most common mechanisms that drive CIN in tumors include merotelic attachments, increased centrosome copy number, and whole genome duplication (Thompson and Compton, 2008; Gordon et al., 2012; Baker et al., 2024), but the cellular mechanisms governing the occurrence of these mitotic errors are not fully understood. The spindle assembly checkpoint (SAC) is a key safeguard that prevents mitotic errors by delaying mitosis in the presence of improper kinetochore-microtubule attachments and other mitotic defects. Although mutations in SAC genes enhance tumorigenesis in animal models, SAC mutations are actually rare in human tumors (Dobles *et al.*, 2000; Baker *et al.*, 2004; Schvartzman *et al.*, 2010).

In this study, we performed a genome-wide CRISPR/Cas9 knockout (KO) screen in that aimed to identify genes and pathways that affect the frequency of or influence the cellular response to chromosomal mis-segregation. The screen was conducted under the treatment with the MPS1/TTK inhibitor NMS-P715, which was designed to uncover genes whose loss either sensitized cells to SAC abrogation or modified the fitness of aneuploid progeny. Our screen identified *PRR14L,* a poorly understood nuclear gene that was previously shown to harbor mutations causing clonality in chronic myelomonocytic leukemia (CMML) (Chase *et al.*, 2019). We further characterized the role of *PRR14L* in cell division by identifying its putative interacting proteins and sensitivity to anti-mitotic compounds of its loss-of-function mutant. Our findings

60 suggest that MPS1 inhibitors may be explored to treat tumors with either loss of function *PRR14L*

61 mutations or FGFR-TACC3 fusions.

62

63 **Results and Discussion**

64

65 **A CRISPR/Cas9 screen to identify enhancers and suppressors of MPS1i**

66 To identify genes that may regulate aneuploidy induction and/or survival, we
67 performed a genome-wide CRISPR/Cas9 KO screen utilizing a previously established
68 NALM-6 pre-B cell lymphoblastic leukemia line, with a doxycycline-inducible Cas9, and
69 the extended-knockout (EKO) sgRNA library harboring 278,754 sgRNAs (Bertomeu *et*
70 *al.*, 2018). Cells were treated for 7 days with doxycycline to induce Cas9 mediated gene
71 KO, followed by a 2 day treatment with either 1 μM NMS-P715, to inhibit MPS1/TTK and
72 induce aneuploidy, or vehicle control. NMS-P715 was subsequently washed out and
73 cells were allowed to recover for 6 days in drug free media prior to analysis (Narkar *et*
74 *al.*, 2021). We then compared the frequency of sgRNAs between DMSO control and
75 NMS-P715-treated population to identify genes which may enhance or suppress the
76 effect of MPS1/TTK inhibition (**Fig. 1A and B**).

77 Analysis of enriched sgRNAs revealed a number of genes that either encode
78 anaphase-promoting complex (APC/C) subunits or regulate APC/C activity. This finding
79 corroborated previous reports showing that a reduction in APC/C activity, which delays
80 mitotic exit, can compensate for a disrupted SAC to limit chromosomal instability (**Fig.**
81 **1C**) (Sansregret *et al.*, 2017). Another subset of suppressor genes encoded protein
82 phosphatase 2A (PP2A) subunits or their regulators, consistent with the idea that loss of
83 PP2A mitigates SAC silencing (Lara-Gonzalez *et al.*, 2021).

84 The depleted sgRNAs identified by our screen affected a more diverse profile of
85 genes (**Fig. 1d**). We identified a number of essential genes (*e.g. DDX3X and NCAPH2*),

some of which also have well-established roles in mitosis (*e.g. BUB1B* and *ZWINT*). We decided to focus further investigation on *PRR14L*, a poorly understood gene hypothesized to play a role in cell division. *PRR14L* encodes a 237 kDa protein previously linked to myeloid neoplasms, PP2A, and PLK1 activity (Chase *et al.*, 2019, 2023; Normandin *et al.*, 2023).

Proximity labeling to identify likely interacting proteins of PRR14L.

To gain insight into the cellular function of *PRR14L*, we used TurboID (Branon *et al.*, 2018; Cho *et al.*, 2020) to identify the proximal proteome of PRR14L. HCT116 cells were generated which stably expressed PRR14L fused to 3xHA-TurboID via a glycine-serine linker (referred to as PRR14L-GS-3xHA-TurboID) and a special control for nuclear localization (3xHA-TurboID-3xNLS). We first validated nuclear localization of the these construct with anti-HA antibodies and biotin labeling. In the spatial control cells with 3xHA-TurboID-3xNLS, we observed nuclear localization of the construct and strong labeling of the nucleoli. In contrast, PRR14L-GS-3xHA-TurboID localized primarily to the nucleoplasm and displayed weak biotin labeling of the nucleoplasm and nucleoli (**Fig. 2B**). To confirm 3xHA-TurboID-3xNLS and PRR14L-GS-3xHA-TurboID label different proximal proteins, we generated cell lysates from untransfected, unlabeled and labeled cells and probed for both the HA-tag and biotinylated proteins (**Fig. 2C**). Western blot analysis revealed notably different biotin-labeling patterns between the two constructs, with strong PRR14L self-labeling and weaker labeling of other proteins.

107 For mass spectrometry analysis, we proceeded with a 4-sample experiment
108 design using a tandem mass tag (TMT) approach (**Fig. 2A**)(Branon *et al.*, 2018). To
109 control for endogenously biotinylated proteins and non-specific binding to the
110 streptavidin beads, we included a no ligase control labeled with 134N. To account for
111 background labeling of nuclear proteins, due to PRR14L's nuclear localization, we
112 included the spatial control, 3xHA-TurboID-NLS, labeled with 133C. Two independent
113 experiments using PRR14L-GS-3xHA-TurboID, were labeled with 133N and 126C
114 respectively (see Materials and Methods for further details).

115 We observed a linear correlation between labeling of the spatial control and both
116 PRR14L independent experiments as expected (**Sup. Fig. 1A and B**). Importantly, the
117 two independent experiments had a strong linear correlation with a R^2 of 0.899 (**Sup.
118 Fig. 1C**). We utilized ER membrane and cell membrane proteins as false positive filters
119 (**Sup. Fig. 1D-G,** see methods).The two sets of filters reduced the potential PRR14L
120 proximal proteome roughly 50-fold (**Sup. Fig. 1H and I**). Overlapping of the two
121 independent experiments yielded the final PRR14L proximal proteome list, where
122 PRR14L itself was the most enriched as expected (**Sup. Fig. 1J**). GO annotation
123 identified several categories of proteins, including protein quality control, nuclear import,
124 and mitochondria (**Sup. Fig. 1K-N**). A subset of proteins found were related to cell
125 division and dephosphorylation (**Fig. 2D, Sup. Fig. 1K**). PRR14L has a C-terminal
126 tantalus domain that is suggested to bind B56-family regulatory subunit of PP2A, and
127 two of these subunits were identified (Serine/threonine-protein phosphatase 2A 56 kDa
128 regulatory subunit alpha and delta isoforms). PRR14L proximity labeling also identified
129 TACC3, which was validated via western blot (**Fig. 2E**). TACC3 is a centrosome and

130 spindle protein that is a substrate of AURKA and thus hypothesized to be regulated by
131 PP2A, as well as a known oncoprotein(Still *et al.*, 1999; Lin *et al.*, 2010; Wong *et al.*,
132 2025).

133

134 ***Loss of PRR14L alters the response of cells to anti-mitotic drugs***

135 To study the cellular function of PRR14L, we generated *PRR14L* knockouts
136 (*PRR14L*$^{-/-}$) in the near diploid HCT116 human colon carcinoma cell line. We chose this
137 cell line because it is chromosomally stable and also adherent, allowing us to more
138 easily visualize mitosis. The success of CRISPR knockout was validated via both
139 genotyping and qPCR quantification of mRNA expression (**Sup. Fig. 2A and B**).
140 Protein-level validation was not successful using commercially available antibodies for
141 PRR14L, due to the presence of off-target antigens and likely also low endogenous
142 expression of the protein (data not shown). As a non-targeting control (*NTC*), we
143 generated monoclonal HCT116 cells transduced with LentiCRISPR v2 carrying a
144 protospacer not predicted to be in the human genome.

145 Given the nuclear localization of PRR14L (Chase *et al.*, 2019), we investigated
146 whether *PRR14L*$^{-/-}$ caused a global change in gene transcription by bulk RNA-
147 sequencing comparing *PRR14L*$^{-/-}$ cells with *NTC* cells. This revealed 375 differentially
148 expressed genes and GO analysis suggested an effect on cell differentiation
149 (Supplementary Tables 1,2). GSEA analysis revealed activation of interferon alpha
150 response and epithelial mesenchymal transition signatures, as well as suppression of
151 the G2/M checkpoint when comparing loss of PRR14L to control (**Sup Fig. 2C).** Further

152 analysis with PROGENy revealed significant upregulation of the WNT pathway in
153 PRR14L knockouts (**Sup Fig. 2D)**. However, the data does not suggest a general role
154 for PRR14L in transcriptional regulation, and it was difficult to conclude whether or not
155 the differential gene expression that we observed were attributable to loss of PRR14L or
156 adaptation to the genetic alteration.

157 The proximity between PRR14L and both PP2A-B56 regulatory subunits and a
158 PP2A substrate led us to hypothesize that PRR14L plays a role in regulating mitosis. To
159 test this, we generated HCT116 *NTC* and HCT116 *PRR14L*$^{-/-}$ cells expressing both
160 H2B-mNeonGreen to label chromatin, and mCherry-CAAX to label the cell membrane.
161 Surprisingly, live cell imaging revealed no significant difference in NEBD to anaphase
162 time between control and *PRR14L*$^{-/-}$ cells (**Fig. 3A**). Additionally, metaphase
163 chromosome spreads revealed no significant difference in chromosome numbers
164 between the control and *PRR14L*$^{-/-}$ cells (**Supplementary Fig. 3A**). These results
165 suggested that under unperturbed conditions, *PRR14L*$^{-/-}$ cells undergo what appear to
166 be normal mitoses.

167 Since PP2A-B56 is known to play a role in SAC silencing (Vallardi *et al.*, 2019),
168 we next tested the strength of the SAC in *PRR14L*$^{-/-}$ cells by treating cells with low dose
169 (25 nM) nocodazole and observing the duration of mitosis. Notably, *PRR14L*$^{-/-}$ cells
170 spent a significantly longer time in mitosis than the control in the presence of low dose
171 nocodazole (**Fig. 3B**). This suggests that either PRR14L contributes to SAC silencing,
172 and/or loss of PRR14L leads to mitotic defects that sensitize cells to nocodazole
173 treatment. If the loss of PRR14L strengthened the SAC, then we would expect *PRR14L*$^{-}$
174 $^{/-}$ cells to resist MPS1/TTK inhibition which weakens the SAC. However, *PRR14L*$^{-/-}$ cells

175 showed more prominent mitotic defects than control cells in the presence of NMS-P715
176 that frequently resulted in highly asymmetric chromatin distribution, with the most
177 extreme case similar to monopolar division that result in a single daughter cell with DNA
178 inheritance (**Fig. 3C and D**). In line with this observation, metaphase chromosome
179 spreads revealed that the ploidy of *PRR14L*$^{-/-}$ cells became near-tetraploid after NMS-
180 P715 treatment (**Sup. Fig. 3B**).

181 It is possible that *PRR14L*$^{-/-}$ cells only show mitotic defects when the SAC is
182 disrupted by MPS1i (Colombo et al., 2010). We thus observed the response of PRR14L^{-}
183 $^{/-}$ cells to ZM447439, an aurora kinase (AURK) inhibitor that disables SAC through an
184 alternative mechanism. Surprisingly, we found that although control cells often fail cell
185 division even with low-dose ZM447439 treatment, this cell division defect is partially
186 suppressed by *PRR14L*$^{-/-}$ (**Fig. 3C, Sup. Fig. 3D**). Thus, loss of PRR14L appears to
187 sensitize cells specifically to MPS1 inhibition but compensate for AURK inhibition.

188

189 ***Mutations affecting the PP2A- PRR14L-TACC3 axis sensitize cells to MPS1i***

190 Given that PRR14L loss of function mutations have been found in CMML and are
191 potentially sufficient for clonality, we asked whether MPS1i can be used to eliminate
192 PRR14L deficient cells using a competition assay. HCT116-NTC cells were stably
193 transfected with mNeonGreen and HCT116-*PRR14L*$^{-/-}$ with mScarlet. These cells were
194 initially mixed with equal proportion and their relative abundance were tracked over 9
195 days in either DMSO or 1 μM NMS-P715 (**Fig. 4A and B**). *PRR14L*$^{-/-}$ cells were
196 significantly more sensitive to MPS1i relative to control (**Fig. 4C**), and this finding also

197 holds for both reversine and AZ-3146, other well-established MPS1/TTKi (**Sup. Fig. 3D**)
198 (Hewitt *et al.*, 2010; Santaguida *et al.*, 2010).

199 Based on findings described above, we propose a preliminary model whereby
200 PRR14L serves as an adaptor protein that facilitates phosphatase access to substrates
201 (**Fig. 4D)**. This model posits that PRR14L acts as a scaffold bringing PP2A-B56 into
202 proximity with TACC3, whose function is regulated by a phosphorylation balance
203 between Aurora A kinase and PP2A. If true, this would suggest that loss of PRR14L
204 could potentially phenocopy TACC3 overactivation due to FGFR-TACC3 gene fusions -
205 driver mutations in cervical cancer, glioblastoma, and NSCLC (Singh *et al.*, 2012;
206 Capelletti *et al.*, 2014; Carneiro *et al.*, 2015). Both genetic alterations - loss of the
207 PRR14L scaffold or FGFR-TACC3 fusion - may converge on TACC3 dysregulation,
208 creating a synthetic lethal vulnerability to MPS1 inhibition. Supporting this idea, analysis
209 of Dependency Map portal revealed that the three cancer cell lines that harbor a FGFR-
210 TACC3 fusion are sensitive to both NMS-P715 and reversine (**Fig. 4E**).

211 In summary, findings of this study provide further insight into the role of PRR14L
212 as a regulator of mitotic fidelity whose function is particularly prominent when MPS1 is
213 inhibited. We hypothesize that PRR14L functions as a scaffold for the PP2A-B56
214 phosphatase, coordinating the dephosphorylation of distinct substrates to ensure proper
215 chromosome segregation. The paradoxical sensitivity to MPS1 and resistance to aurora
216 kinase inhibition suggests a dual role for PRR14L. On one hand, its loss impairs PP2A-
217 B56 mediated SAC silencing, leading to prolonged arrest in nocodazole. On the other
218 hand, PRR14L appears critical for maintaining spindle integrity, likely via TACC3
219 regulation. When MPS1 is inhibited, the SAC is bypassed, and this underlying spindle

220 fragility leads to catastrophic errors, overwhelming the cell despite the potentially
221 hyperactive SAC machinery. Our results point to a potential vulnerability toward MPS1
222 inhibitors with driver mutations impact the PP2A- PRR14L-TACC3 axis and suggest a
223 testable therapeutic strategy for such genetically defined cancers.

224

225 **Materials and Methods**

REAGENT or RESOURCE	SOURCE	IDENTIFIER
Antibodies		
Mouse monoclonal anti-alpha Tubulin [DM1A]	Cell Signaling Technology	Cat#3873S; RRID:AB_1904178
Rabbit polyclonal anti-CEP152	Abcam	Cat# ab183911; RRID:AB_3106957
Rabbit monoclonal anti-TACC3 [EPR7756]	Abcam	Cat# ab134154; RRID: AB_3492052
Mouse monoclonal anti-gamma Tubulin [GTU-88]	Sigma-Aldrich	Cat#T6557; RRID:AB_477584
Rabbit polyclonal anti-PRR14L	Atlas Antibodies	Cat#HPA062645; RRID:AB_2684817
Rabbit polyclonal anti-C22ORF30	Origene	Cat#TA331394; RRID: AB_3492053
Rabbit monoclonal anti-HA-tag	Cell Signaling Technology	Cat#3724S; RRID: AB_1549585
Goat anti-Rabbit IgG (Heavy chain), Superclonal Recombinant Secondary Antibody, Alexa Fluor 488	Invitrogen	Cat#A27034; RRID:AB_2536097
Goat anti-Mouse IgG (H+L), Superclonal Recombinant Secondary Antibody, Alexa Fluor 488	Invitrogen	Cat#A28175; RRID:AB_2536161
Goat anti-Rabbit IgG (H+L) Cross-Adsorbed Secondary Antibody, Alexa Fluor 568	Invitrogen	Cat#A-11011; RRID:AB_143157
Goat anti-Mouse IgG (H+L) Cross-Adsorbed Secondary Antibody, Alexa Fluor 568	Invitrogen	Cat#A-11004; RRID:AB_2534072
Goat anti-Rabbit IgG (Heavy chain), Superclonal Recombinant Secondary Antibody, Alexa Fluor 647	Invitrogen	Cat#A27040; RRID: AB_2536101
Goat anti-Mouse IgG (H+L), Superclonal Recombinant Secondary Antibody, Alexa Fluor 647	Invitrogen	Cat#A55060; RRID: AB_2921068
IRDye 680RD Goat anti-Rabbit IgG Secondary Antibody	LICORbio	Cat#926-68071; RRID: AB_10956166
IRDye 680RD Goat anti-Mouse IgG Secondary Antibody	LICORbio	Cat#926-68070; RRID:AB_10956588
IRDye 800CW Goat anti-Rabbit IgG Secondary Antibody	LICORbio	Cat#926-32211; RRID:AB_621843
IRDye 800CW Goat anti-Mouse IgG Secondary Antibody	LICORbio	Cat#926-32210; RRID:AB_621842
Chemicals, peptides, and recombinant proteins		
NMS-P715	Calbiochem	475949; CAS: 1202055-32-0
Reversine	Selleckchem	S7588; CAS: 656820-32-5
AZ-3146	Selleckchem	S2731; CAS: 1124329-14-1
ZM 447439	Selleckchem	S1103; CAS: 331771-20-1
PMSF Protease Inhibitor	Thermo Scientific	36978; CAS: 329-98-6
Pierce Universal Nuclease for Cell Lysis	Thermo Scientific	88700
Alisertib (MLN8237)	Selleckchem	S1133; CAS: 1028486-01-2

Nocodazole	Sigma-Aldrich	SML1665; CAS: 31430-18-9
Paclitaxel	Sigma-Aldrich	T7191; CAS: 33069-62-4
Doxycycline hyclate	Sigma-Aldrich	D5207; CAS: 24390-14-5
Hoechst 33342 trihydrochloride	Santa Cruz Biotechnology	200908; CAS: 23491-52-3
Alt-R S.p. Cas9 Nuclease V3	IDT	1081059
Critical commercial assays		
DNEasy Blood & Tissue Kit	Qiagen	69504
SE Cell Line 96-well Nucleofector Kit	Lonza	V4SC-1096
PureLink Genomic DNA Mini Kit	Invitrogen	K182001
PureLink DNAse Set	Invitrogen	12185010
High-Capacity cDNA Reverse Transcription Kit	Applied Biosystems	4368814
PerfeCTa SYBR Green SuperMix	Quantabio	95054
SiR-Tubulin Kit	Cytoskeleton, Inc.	CY-SC002
QIAquick Gel Extraction Kit	QIAGEN	28704
NEBuilder HiFi DNA Assembly Master Mix	New England Biolabs	E2621
NucleoSpin Plasmid Transfection-grade, Mini kit for ultrapure plasmid DNA	MACHEREY-NAGEL	740490
Plasmid Plus Midi Kit	QIAGEN	12943
Lipofectamine 3000 Transfection Reagent	Invitrogen	L3000001
Pierce BCA Protein Assay Kits	Thermo Scientific	23225
PureLink RNA Mini Kit	Invitrogen	12183018A
Deposited data		
Raw mass spectrometry data	ProteomeXchange Consortium via the PRIDE partner repository	PXDXXXXXX
RNA-sequencing data	GEO	GSEXXXXXX
Experimental models: Cell lines		
NALM-6	Laboratory of Mike Tyers	
NALM-6 pCW-Cas9	Laboratory of Mike Tyers(Bertomeu *et al.*, 2018)	
NALM-6 PRR14L$^{-/-}$ Clone 5-3 (monoclonal)	This study	
NALM-6 PRR14L$^{-/-}$ Clone 6-8 (monoclonal)	This study	
HCT116	Laboratory of Bert Vogelstein	CCL-247
HCT116 NTC (monoclonal)	This study	
HCT116 NTC mNeonGreen (polyclonal)	This study	
HCT116 NTC H2B-mNeonGreen mCherry-CAAX (polyclonal)		
HCT116 PRR14L$^{-/-}$ Clone A3 (monoclonal)	This study	
HCT116 PRR14L$^{-/-}$ Clone A3 mScarlet (polyclonal)	This study	

HCT116 PRR14L$^{-/-}$ Clone A3 H2B-mNeonGreen mCherry-CAAX (polyclonal)	This study	
HCT116 PIKFYVE$^{-/-}$ Clone C2 (monoclonal)	This study	
HCT116 PIFKYVE$^{-/-}$ Clone C2 mScarlet (polyclonal)	This study	
HCT116 mNeonGreen (polyclonal)	This study	
HCT116 H2B-mNeonGreen mCherry-CAAX (polyclonal)	This study	
HCT116 H2B-mCherry (polyclonal)	This study	
HCT116 PRR14L$^{-/-}$ Clone 6-7 (monoclonal)	This study	
HCT116 PRR14L$^{-/-}$ Clone 6-7 mScarlet (polyclonal)	This study	
HCT116 PRR14L$^{-/-}$ Clone 6-7 H2B-mNeonGreen mCherry-CAAX (polyclonal)	This study	
HCT116 PRR14L$^{-/-}$ Clone 6-7 H2B-mCherry (polyclonal)	This study	
HCT116 PRR14L$^{-/-}$ Clone 6-10 (monoclonal)	This study	
HCT116 PRR14L$^{-/-}$ Clone 6-10 mScarlet (polyclonal)	This study	
HCT116 PRR14L$^{-/-}$ Clone 6-10 H2B-mNeonGreen mCherry-CAAX (polyclonal)	This study	
HCT116 PRR14L$^{-/-}$ Clone 6-10 H2B-mCherry (polyclonal)	This study	
hTERT RPE-1	Laboratory of Siew Cheng Phua	CRL-4000
hTERT RPE-1 TetON-PRR14L-TurboID (polyclonal)	This study	
hTERT RPE-1 PRR14L$^{-/-}$ Clone 5-9 (monoclonal)	This study	
hTERT RPE-1 PRR14L$^{-/-}$ Clone 5-9 TetON-PRR14L-TurboID (polyclonal)	This study	
hTERT RPE-1 PRR14L$^{-/-}$ Clone 5-22 (monoclonal)	This study	
293T	ATCC	CRL-3216
LentiX293T	Takara Bio	632180
HEK293FT	Invitrogen	R70007
Oligonucleotides		
Alt-R CRISPR-Cas9 crRNA targeting PRR14L (Azl_crR_005): TCCACTAGCCCACATCGCCC	IDT	
Alt-R CRISPR-Cas9 crRNA targeting PRR14L (Azl_crR_006): CTGTACCACGGCAGACATGG	IDT	
Alt-R CRISPR-Cas9 tracrRNA, ATTO 550	IDT	1075928
ON-TARGETplus Non-targeting Pool	Horizon Discovery	D-001810-10-05
On-TARGETplus Human PPP2CA (5515) siRNA – SMARTpool	Horizon Discovery	L-003598-01-0005
ACTB qPCR Primer (Fwd): GGATCAGCAAGCAGGAGTATG	IDT	
ACTB qPCR Primer (Rev): AGAAAGGGTGTAACGCAACTAA	IDT	
PRR14L qPCR Primer (Fwd): GCTACAAGCGCCTCAGATATAA	IDT	
PRR14L qPCR Primer (Rev): CCATCCACTAGCTGCCAAATA	IDT	
Recombinant DNA		
pBOB-EF1-FastFUCCI-Puro	Koh et al.(Koh *et al.*, 2017)	Addgene #86849
pBOB-EF1-Neon-Puro	This study	
pBOB-EF1-mScarlet-Puro	This study	

pMD2.G	Gift from Didier Trono	Addgene #12259
pRSV-Rev	Gift from Didier Trono	Addgene #12253
pMDLg/pRRE	Gift from Didier Trono	Addgene #12251
pLV-H2B-Neon-T2A-mCherry-CAAX	Johnson et al.(Johnson *et al.*, 2024)	
pBrain-GFP-TACC3KDP-shTACC3	Booth et al.(Booth *et al.*, 2011)	Addgene #59356
3xHA-TurboID-NLS_pCDNA3	Branon et al.(Branon *et al.*, 2018)	Addgene #107171
pPB-cT3G-cERP2-NR5A1	Smela et al.(Smela *et al.*, 2023)	Addgene #192915
pDonor-tBFP-NLS-Neo (Universal)	Katoh et al.(Katoh *et al.*, 2017)	Addgene #80767
pDonor-PRR14L-GS-3xHA-TurboID-BSD	This study	
pPB-cT3G-CERP2(BSD)-PRR14L-GS-3xHA-TurboID	This study	
pPRR14L-GS-Neon-FLAG	This study	
pPRR14L(1-1487)-GS-Neon-FLAG	This study	
pPRR14L(1488-2151)-GS-Neon-FLAG	This study	
pLenti6-H2B-mCherry	Pemble et al.(Pemble *et al.*, 2017)	Addgene #89766
Lenti-Centrin1-GFP	Gift from Alexey Khodjakov	
pRSETB/mStayGold	Ando et al.(Ando *et al.*, 2024)	Addgene #212017
lentiCRISPR v2	Sanajana et al.(Sanjana *et al.*, 2014)	Addgene #52961
lentiCRISPR v2-NTC	This study	
lentiCRISPR v2-PRR14L	This study	
lentiCRISPR v2-PIKFYVE	This study	
psPAX2	Gift from Didier Trono	Addgene #12260
Software and algorithms		
Fiji	Schneider et al.(Schneider *et al.*, 2012)	https://imagej.net/software/fiji/
R, version 4.4.0	R Core Team (2024)	https://www.R-project.org/
RStudio, version 2024.04.1	RStudio Team (2024)	
ICE CRISPR Analysis Tool	Conant et al.(Conant *et al.*, 2022)	
FlowJo	FlowJo LLC	https://www.flowjo.com/
Zen Blue, version 3.5	Zeiss	
ggplot2, version 3.5.1	Wickham et al.(Wickham, 2016)	
Other		
Puromycin Dihydrochloride	Gibco	A1113803
Blasticidin S HCl (10 mg/mL)	Gibco	A1113903
RPMI 1640 Medium	Gibco	11875093
Fetal Bovine Serum, Value, heat inactivated, OneShot format	Gibco	A5209501

Fetal Bovine Serum, Tet system approved, USDA-approved regions, OneShot format	Gibco	A4736301
Penicillin-Streptomycin (10,000 U/mL)	Gibco	15140122
DMEM, high gluose	Gibco	11965092
DMEM/F-12	Gibco	11320033
Hygromycin B (50 mg/mL)	Gibco	10687010
GlutaMAX Supplement	Gibco	35050061
MEM Non-Essential Amino Acids Solution (100x)	Gibco	11140050
Lenti-X Concentrator	Takara	631232
Sodium Pyruvate (100 mM)	Gibco	11360070
Nunc Lab-Tek Chambered Coverglass	Thermo Scientific	155411
FluoroBrite DMEM	Gibco	A1896701
µ-slide 8 well	ibidi	80826
µ-slide 8 well high Glass Bottom	ibidi	80807
Glass Base Dish 27 mm	iwaki	3970-035
KaryoMAX Colcemid Solution in PBS	Gibco	15212012
Q5 High-Fidelity DNA Polymerase	New England Biolabs	M0491
Platinum SuperFi II Green PCR Master Mix	Invitrogen	12369010
NEB 5-alpha Competent E. coli (High Efficiency)	New England Biolabs	C2987
NEB Stable Competent E. coli (High Efficiency)	New England Biolabs	C3040
ProLong Gold Antifade Mountant	Invitrogen	P36930
Fibronectin (pure)	Roche	11051407001
D-Biotin	Invitrogen	B20656
RIPA Lysis and Extraction Buffer	Thermo Scientific	89900
Protease/Phosphatase Inhibitor Cocktail (100X)	Cell Signaling Technology	5872
Laemmli SDS sample buffer, reducing (6x)	Alfa Aesar	J61337
Precision Plus Protein Dual Color Standards	BIORAD	1610374
Spectra Multicolor High Range Protein Ladder	Thermo Scientific	26625
4-20% Mini-PROTEAN TGX Precast Protein Gels, 10-well, 50 µL	BIORAD	4561094
4-20% Mini-PROTEAN TGX Precast Protein Gels, 15-well, 15 µL	BIORAD	4561096
Trans-Blot Turbo Mini 0.2 µm Nitrocellulose Transfer Packs	BIORAD	1704158
Streptavidin, Alexa Fluor 488 conjugate	Invitrogen	S11223
Streptavidin Protein, DyLight 680	Invitrogen	21848
Opti-MEM I Reduced Serum Media	Gibco	31985070

226

227 **Cell culture**

228 NALM-6 cells were grown at 37 ˚C with 5% CO_2 in RPMI 1640 supplemented with 10%
229 heat-inactivated (HI) fetal bovine serum (FBS) and 100 U/mL Penicillin/Streptomycin
230 (Pen/Strep). HCT116 cells were grown at 37 ˚C with 5% CO_2 in DMEM supplemented

231 with 10% HI FBS and 100 U/mL Pen/Strep. hTERT RPE-1 cells were grown at 37 ˚C
232 with 5% CO_2 in DMEM/F12 supplemented with 10% HI FBS and 10 µg/mL Hygromycin
233 B. 293T cells were grown at 37 ˚C with 5% CO_2 in DMEM supplemented with 10% HI
234 FBS, 100 U/mL Pen/Strep, and 1% GlutaMAX. HEK293FT cells were grown at 37 ˚C
235 with 5% CO_2 in DMEM supplemented with 10% HI FBS. LentiX293T cells were grown at
236 37 ˚C with 5% CO_2 in DMEM supplemented with 10% HI FBS, 1% GlutaMAX, 1x MEM
237 non-essential amino acids, 1 mM Sodium Pyruvate, and 50 U/mL Pen/Strep.
238 Mycoplasma testing was completed every 3-6 months to ensure cultures were free of
239 mycoplasma contamination.

240 **Genome-wide pooled CRISPR/Cas9 Screen**

241 The genome-wide pooled CRISPR/Cas9 screen was completed as previously
242 described(Bertomeu *et al.*, 2018; Normandin *et al.*, 2023). In brief, a custom sgRNA
243 library was used comprised of 233,268 sgRNAs that target 19,084 protein coding genes
244 and 17,139 alternatively spliced exons. Each gene was targeted by approximately 10
245 sgRNAs. Noise was controlled for via 2,043 non-targeting sgRNAs. A doxycycline-
246 inducible Cas9 clone of NALM-6 was used. The two conditions that were compared
247 were vehicle control (DMSO, 1:1000) and 1 µM NMS-P715. After doxycycline induction
248 for 1 week, DMSO and 1 µM NMS-P715 treatment were started Day 0 of the screen,
249 and washed out Day 2. Cells were collected on both Day 2 and Day 8 for gDNA
250 extraction and NGS.

251 **Generation of monoclonal KO cell lines**

252 Two independent methods were used to generate monoclonal KO cell lines.

253 Lentivirus method:

254 HCT116 PRR14L$^{-/-}$ clone A3 was generated using the lentiCRISPRv2 system. In
255 brief, lentiCRISPRv2-PRR14L was cloned using the protospacer 5'-
256 TCTGCTCTACCCTCTAATGG-3', and lentiCRISPRv2-PIKFYVE was cloned using the
257 protospacer 5'-ACATATGTTCGGTTAGCCTG-3'. Lentiviral particles were generated and
258 collected via Lipofectamine-based transient transfection of HEK293FT cells with the
259 following three plasmids in 1:1:1 molar ratio: lentiCRISPRv2, pMD2.G, and psPax2.
260 HCT116 cells were transduced with lentiviral particles at a MOI of 0.5-1, and then
261 underwent selection with 1 µg/mL Puromycin for 3 days followed by single cell sorting.
262 Genomic DNA (gDNA) was extracted from single cell clones using DNEasy Blood and
263 Tissue Kit (Qiagen) and amplified using the following primers: PRR14L: FWD 5'-
264 CTGTTGCTACCATCCCCAGA-3' | REV 5'-GAGACCACTTGAGGAAAGCCA-3'. PCR
265 product was purified and submitted for sanger sequencing using the primer: 5'-
266 CCACTTGAGGAAAGCCAGCT-3'. Sequencing data was analyzed using the ICE
267 analysis tool to assess for successful gene knockout via frameshift mutation(Conant *et*
268 *al.*, 2022). Control cells referred to as "HCT116 NTC" were generated in the exact same
269 manner except a non-targeting protospacer was used with the sequence 5'-
270 gccccgccgccctcccctcc-3'.

271 **Lentivirus Generation and Transduction**

272 Second generation lentivirus generation:

273 2 x 10^6 HEK293FT cells were seeded in a T-25 flask. After 24 hrs, cells were
274 transfected with the transfer plasmid, pMD2.G, and psPax2 in a 1:1:1 molar ratio using

275 Lipofectamine 3000. 48 hrs after transfection, lentivirus supernatant was collected,
276 aliquoted, and frozen at -80 ˚C for future use.

277 Third generation lentivirus generation:

278 Third generation lentivirus was produced following a previously published
279 protocol with a few modifications25. LentiX293T cells were used for lentivirus
280 production, and Lenti-X concentrator was used to concentrate lentiviral supernatants 5
281 to 10-fold. Concentrated lentiviral pellets were resuspended in DPBS and frozen at -
282 80 ˚C for future use.

283 Lentivirus transduction:

284 Lentivirus aliquots were warmed quickly using a 37 ˚C water bath for 2-3 min.
285 Cells were transduced with a mixture of fresh media, lentivirus supernatant, and 10
286 µg/mL polybrene for 48 hrs. This was followed by either antibiotic selection or
287 fluorescent-activated cell sorting (FACS) to obtain polyclonal and/or monoclonal cell
288 lines.

289 **Competition Assay**

290 Polyclonal fluorescent populations of competing cell lines were obtained by lentiviral
291 transduction of cell lines with pBOB-EF1-Neon-Puro or pBOB-EF1-mScarlet-Puro. Cells
292 were seeded at equal cell number on Day 0 in triplicate for each day to be measured,
293 *i.e.*, for a 9-day experiment with two different drug treatments, a total of 30 wells were
294 seeded initially. Media was changed to fresh media with drug treatment or control on
295 Day 1. Drug treatments were washed out on Day 3. Cells were passaged every 2 days
296 if the confluency was observed to be >75%; otherwise, a media change was completed.

297 Population numbers were measured using flow cytometry using either an Attune NxT
298 Flow Cytometer or a Sony SH800. Data were analyzed using FlowJo and plots were
299 generated with Rstudio and ggplot2.

300 **qPCR Profiling and Analysis**

301 RNA was extracted from cells using PureLink RNA Mini Kit in combination with
302 PureLink DNase Set. RNA concentration was measured with Nanodrop and then
303 normalized to 100 ng/μL with RNase free water. cDNA was generated using High
304 Capacity cDNA Reverse Transcriptase Kit. qPCR was completed using PerfeCTa SYBR
305 Green Supermix. Fold change was calculated using ddCt method with ACTB and/or
306 GAPDH as a control, and plots were generated with Rstudio and ggplot2.

307

308 **RNA Sequencing and Data Analysis**

309 Library Preparation and Sequencing Total RNA was extracted from HCT116 NTC and
310 PRR14L-/- (Clone A3) cells using the PureLink RNA Mini Kit (Invitrogen) with on-column
311 DNase treatment (PureLink DNase Set, Invitrogen), according to the manufacturer's
312 instructions. Stranded RNA sequencing library preparation and high-throughput
313 sequencing were performed by BGI Genomics (Hong Kong). Paired-end sequencing
314 (PE100) was conducted on the DNBSEQ platform.

315

316 Preprocessing and Quantification Raw FASTQ files were processed by BGI using their
317 internal analysis platform, Dr. Tom. Briefly, reads were quality-controlled, aligned to the

human reference genome (Ensembl release 105), and gene expression levels were quantified as raw read counts.

Differential Gene Expression (DGE) Analysis Differential gene expression analysis was performed in R (v4.4.0) using the DESeq2 package (Love et al., 2014). To improve visualization and ranking, log2 fold changes (LFC) were shrunk using the apeglm method (Zhu et al., 2019). Genes were considered significantly differentially expressed if they met the criteria of an FDR-adjusted p-value (padj) < 0.05 and an absolute LFC > 1 (2-fold change). Gene Set Enrichment Analysis (GSEA) GSEA was performed using the clusterProfiler package (Wu et al., 2021) against the MSigDB Hallmark gene sets, retrieved via msigdbr. Genes were ranked by the Wald statistic obtained directly from the DESeq2 results. Pathway activities were inferred using PROGENy (Schubert et al., 2018). VST-normalized expression data, aggregated to gene symbols, were used as input and pathway scores were calculated based on the expression of the top 100 footprint genes per pathway. Differential pathway activities between KO and NTC samples were determined by applying a robust Student's t-test to the inferred activity scores. Significance was determined by an FDR-adjusted p-value < 0.05.

Live Cell Imaging

Live cell imaging was done via two methods based on location of experiment.

1. Cells were seeded in Nunc Lab-Tek chambered cover glass 2 days prior to imaging. Prior to the beginning of imaging, media was changed to fresh

340 FluoroBrite DMEM supplemented with HI FBS and Pen/Strep, with or without
341 drug treatment. Imaging was completed on a Zeiss LSM 780 laser scanning
342 confocal microscope with an environmental chamber kept at 37 ˚C with 5% CO_2
343 using a 63x oil-immersion objective (NA 1.4). For most independent experiments,
344 4-6 positions per genotype were imaged at once, with a 3 min time interval, and a
345 15-20 slice Z-stack with 1 µm slices. Deviations from this are mentioned in figure
346 captions. Images were processed in ImageJ, with adjustments to color balance
347 and cropping of selected cells of interest. Judgment of mitotic errors and/or
348 mitotic outcome was done manually. Any fluorescence intensity quantification
349 was done on unprocessed images.

350 2. Cells were seeded in ibidi µ-slides 2 days prior to imaging. 12 hrs prior to the
351 start of imaging, media was changed to fresh FluoroBrite DMEM supplemented
352 with HI FBS and 1x GlutaMAX. If drug treatment(s) were used, they were added
353 2 hrs prior to imaging in fresh FluoroBrite DMEM supplemented with HI FBS, 1x
354 GlutaMax, and 50 nM SiR-Tubulin. Imaging was completed on one of three
355 microscopes: Zeiss LSM 980 laser scanning confocal microscope with
356 environmental chamber, 63x oil-immersion objective (NA 1.4), in either confocal
357 mode, CO-8Y mode, or SR mode; Oxford Instruments BC43 spinning disk
358 confocal microscope with environmental chamber, 60x oil-immersion objective
359 (NA 1.42), and deconvolution completed with Imaris software; Zeiss Lattice
360 Lightsheet 7 with environmental chamber, water-based objective (NA 1.0), and
361 deskewing, cover glass transformation, and deconvolution was completed using
362 Zen Blue software.

363 **Metaphase Spreads**

364 Cells were treated with 100 ng/mL of colcemid for 6 hrs and then collected. Cell pellets
365 were resuspended in PBS, and then incubated with pre-warmed 75 mM KCl for 10 min
366 to induce cell swelling. Swollen cells were fixed with a solution of 3:1 methanol:glacial
367 acetic acid overnight at 4 ˚C. Fixed cells were dropped onto pre-humidified glass slides,
368 and then slides were dried by warming them to 65 ˚C on a hot plate for 20 min. Slides
369 were mounted with ProLong Gold Antifade Mountant with DAPI followed by the addition
370 of a coverslip and overnight curing at room temperature. Imaging was completed on a
371 Nikon TiE-Eclipse epifluorescence microscope with 60x oil immersion objective.
372 Chromosome number was recorded manually for each metaphase spread using the cell
373 counter plugin in ImageJ.

374 **Plasmid cloning**

375 A list of all plasmids used in this study can be found in the Recombinant DNA section of
376 the materials list. All plasmid generation was completed via Gibson assembly (Gibson *et*
377 *al.*, 2009). Primers to generate new plasmids were designed using
378 https://nebuilder.neb.com/#!/. For assemblies of 2 or 3 fragments, primers were
379 designed with 20 bp overlaps. For assemblies of 4+ fragments, primers were designed
380 with >24 bp overlaps. For assemblies requiring the addition of small fragments (e.g. GS
381 linker, T2A sequence), small single-stranded oligonucleotide donors (ssODNs) were
382 used. PCRs were completed using either Q5 Polymerase or Platinum SuperFi
383 Polymerase. Products were run on 1% agarose gels, and then bands of the correct size
384 were extracted using QIAquick Gel Extraction Kit. Gibson assembly was performed
385 using NEBuilder HiFi DNA Assembly Master Mix, and products were transformed into

386 either NEB 5-alpha Competent E. coli or NEB Stable Competent E. coli. Multiple single
387 colonies were picked to inoculate miniprep cultures, and plasmid DNA was extracted
388 using NucleoSpin Plasmid Transfection-grade, Mini kit. Plasmids were submitted for
389 sanger sequencing to confirm assembly junctions. Confirmed plasmids were then re-
390 picked to inoculate midiprep cultures, and plasmid DNA was extracted using QIAGEN
391 Plasmid Plus Midi Kit. Midipreps were then submitted for sequencing of all functional
392 genetic components (i.e. promoter, transgene, etc.) before being used for cell
393 transfection.

394 **Transient Transfection**

395 Transient transfection was carried out using Lipofectamine 3000, following the
396 manufacturer's instructions with a few modifications. The amount of OptiMEM Reduced
397 Serum Media used was doubled, and prior to transfection the same amount of OptiMEM
398 to be added was removed from cell culture. Lipofectamine 3000:P3000 Reagent::1.18:1.
399 P3000 Reagent:Plasmid DNA::2 µL:1 µg. Cells were analyzed between 24-72 hrs after
400 transfection.

401 **TurboID Immunofluorescence Validation**

402 The following protocol is based on previously published work with slight
403 modifications(Cho *et al.*, 2020). Ibidi µ-slides 8-well were coated with 200 µL of 50
404 µg/mL fibronectin in DPBS per well for 30 min. $3.6x10^4$ 293T cells were seeded per well.
405 After 24 hours, TurboID constructs were transfected using Lipofectamine 3000. After
406 another 24 hours, media was replaced with fresh warm cDMEM supplemented with 50
407 µM biotin for either 10 min (3xHA-TurboID-3xNLS) or 20-30 min (PRR14L-GS-3xHA-

408 TurboID). Labeling was stopped with 5x ice cold DPBS washes followed by fixation with
409 4% PFA in PBS at RT for 10-15 min. Blocking and permeabilization was completed
410 simultaneously with 1 hr incubation with AbdIl (2% BSA, 0.1% Triton X-100, in TBS).
411 1˚ antibody against HA-tag was incubated overnight (O/N) at 4 ˚C diluted 1:1,200 in
412 AbdIl. Cells were washed 3x with TBST (0.1% Triton X-100 in TBS) followed by 1hr
413 room temperature (RT) incubation with 2˚ antibodies diluted in AbdIl: anti-rabbit
414 conjugated with Alexa Fluor 568 (1:1,000) and Streptavidin conjugated with Alexa Fluor
415 488 (1:1,000). Cells were washed 1x with TBST, followed by counterstaining with
416 Hoechst 33342 in TBST for 5 min RT, followed by 1x TBST rinse, 1x TBST wash, and
417 cells were imaged in 1x TBS buffer.

418 **Western Blot for TurboID Validation**

419 $3x10^5$ 293T cells were plated per well in 6-well plates. After 24 hours, TurboID
420 constructs were transfected using Lipofectamine 3000. After another 24 hours, media
421 was replaced with fresh warm cDMEM supplemented with 50 μM biotin for either 10 min
422 (3xHA-TurboID-3xNLS) or 20-30 min (PRR14L-GS-3xHA-TurboID). Labeling was
423 stopped with 5x ice cold DPBS washes followed by use of 1mL ice cold DPBS to detach
424 cells and collect cell pellets. Cell pellets were resuspended in 100 μL of RIPA buffer
425 supplemented with 1x protease and phosphatase inhibitor, 1 mM PMSF, and Pierce
426 universal nuclease for cell lysis, and lysed for 20-40 min on ice with thorough pipetting
427 every 10 min. Lysates were clarified by centrifugation at 14,000 rcf for 15 min at 4 ˚C. 80
428 μL of supernatant was collected and 5 μL was used for BCA protein quantification.
429 Protein concentration was normalized across samples and then combined with 6x
430 Laemmli sample buffer and boiled for 10 min. Samples were loaded onto Mini-

431 PROTEAN TGX precast protein gels, 4-20%, either 15x15 µL wells or 10x50 µL wells
432 with either Precision Plus Dual Protein Color Standards or Spectra Multicolor High
433 Range Protein Ladder for molecular weight ladder. Samples were transferred onto 0.2
434 µm nitrocellulose blots using the Trans-Blot Turbo transfer system, mixed molecular
435 weight protocol. Blots were blocked with Intercept (TBS) Blocking buffer for 1 hr at RT
436 followed by O/N incubation with 1˚ Ab (anti-HA). Blots were washed 4x with TBST (0.1%
437 Tween-20 in TBS) followed by 1 hr incubation with 2˚ Ab diluted in 1:1::blocking
438 buffer:TBST – Streptavidin Dylight 680 (1:5,000) and IRDye 800CW Goat anti-Rabbit
439 IgG Secondary Antibody (1:20,000). Blots were washed again with 4x TBST followed by
440 2x TBS, and then imaged on an Odyssey CLx Imager.

441 **TMT Mass Spectrometry**

442 2.25×10^6 293T cells were plated in T-75 flasks, two T-75 flasks per independent
443 experiment. After 24 hours, TurboID constructs were transfected using Lipofectamine
444 3000. After another 24 hours, media was replaced with fresh warm cDMEM
445 supplemented with 50 µM biotin for either 10 min (No ligase control and 3xHA-TurboID-
446 3xNLS) or 30 min (PRR14L-GS-3xHA-TurboID). Labeling time of the PRR14L construct
447 was extended to compensate for the weaker labeling by the PRR14L fusion construct
448 relative to control. Labeling was stopped with 5x ice cold DPBS washes followed by use
449 of 7.5 mL ice cold DPBS per flask to detach cells and collect cell pellets. Cell pellets
450 were resuspended in 1.5 mL of RIPA buffer supplemented with 1x protease and
451 phosphatase inhibitor, 1 mM PMSF, and Pierce universal nuclease for cell lysis, and
452 lysed for 50 min on ice with thorough pipetting every 10 min. Lysates were clarified by
453 centrifugation at 14,000 rcf for 15 min at 4 ˚C. Streptavidin magnetic beads were

454 washed twice with 1 mL RIPA. 15 µL of lysate was retained as input, and the remainder
455 was loaded on the streptavidin beads O/N rotating at 4 ˚C. 15 µL of flowthrough was
456 collected per sample, and then beads were washed with: 2x 1 mL RIPA (2 min per
457 wash), 1x 1mL KCl (2 min), 1x 1mL 100 nM Na_2CO_3 (10 sec), 1x 1mL 2M urea in 10 mM
458 Tris-HCl pH 8.0 (10 sec), 2x 1 mL RIPA (2x 2min). The beads were resuspended in 1mL
459 RIPA, transferred to fresh microcentrifuge tubes, and then flash frozen in liquid nitrogen
460 and stored at -80 ˚C until further processing.

461 For each sample 100 µg of protein was added to a 10 kDa ultrafiltration tube, and
462 volume was normalized across samples. Samples were centrifuged at 20 ˚C, 12,000 rcf
463 for 20 min. 100 µL of 0.5M TEAB was added to samples and then centrifuged at 20 ˚C
464 12,000 rcf for 20 min (3x). Samples were subjected to Trypsin digestion at 37 ˚C for 4
465 hours. Peptide solution was concentrated and desalted, and the collected peptide
466 fractions were freeze-dried. For peptide labeling, each tube of TMT (0.8 mg) was
467 dissolved in 41 µL acetonitrile and shaken for more than 1 min. Peptide fragments were
468 resuspended in 0.1M TEAB to a concentration of 3.74 µg/µL. 100 µg of peptide was
469 labeled with 41 µL of TMT reagent for 2 hr at room temperature, ensuring pH was
470 between 7-8.

471 For peptide fractionation the Shimadzu LC-20AB liquid phase system was used
472 with a 5 µm 4.6x250mm Gemini C18 column for liquid phase separation of the sample.
473 Dried peptide samples were reconstituted with mobile phase A (5% acetonitrile pH 9.8)
474 and injected, eluting at a flow rate of 1 mL/min with the following gradients: 5% mobile
475 phase B (95% acetonitrile, pH 9.8) for 10 min. 5% to 35% mobile phase B for 40 min.
476 35% to 95% mobile phase B for 1 min, mobile phase B for 3 min, and 5% mobile phase

477 B for 10 min. The elution peak was monitored at a wavelength of 214 nm and one
478 component was collected per minute, and the samples were combined according to the
479 chromatography elution peak map to obtain 20 fractions, which were then freeze-dried.

480 For HPLC the dried peptide samples were reconstituted with mobile phase A (2%
481 acetonitrile, 0.1% formic acid), centrifuged at 20,000 rcf for 10 min, and the supernatant
482 was used for injection. Separation was performed using a Easy-nLC 1200, followed by a
483 tandem self-packed C18 column (75 μm internal diameter, 1.9 μm column size, 25 cm
484 column length) and separated at a flow rate of 200 nL/min using the following gradient:
485 0 – 3 min, 5% mobile phase B (80% acetonitrile, 0.1% formic acid); 3 – 45 min, mobile
486 phase B was linearly increased from 8 to 44%; 45-50 min, mobile phase B increased
487 from 44 to 60%; 50-53 min, mobile phase B rose from 60 to 100%; 53-60 min, 80%
488 mobile phase B. The nanoliter liquid phase separation was directly connected to the
489 mass spectrometer.

490 For mass spectrometry detection, the peptides separated by HPLC were ionized
491 by a nanoESI source and then passed to a tandem mass spectrometer Orbitrap
492 Exploris 480 for DDA mode detection. Parameters included: ion source voltage = 1.9
493 kV; MS1 mass spectrometer scanning range was 350-1,600m/z; resolution was set to
494 60,000; MS2 starting m/z was fixed at 100; resolution was 15,000. The ion screening
495 conditions for MS2 fragmentation were: charge 2+ to 7+, and the first 30 parent ions
496 with peak intensity exceeding $2x10^4$. Ion fragmentation mode was HCD, and the
497 fragment ions were detected in Orbitrap. The dynamic exclusion time was set to 30
498 seconds. The automatic gain control was set to: MS1 300%, MS2 standard.

Mass spectrometry analysis was completed using Spectrum Mill MS Proteomics software as well as R.

To distinguish specific proximal proteins from abundant nuclear background, we employed a filtering strategy based on a custom False Positive Identification (FPI) rate, calculated against curated lists of proteins from irrelevant subcellular compartments (e.g., ER membrane, cell membrane) obtained from UniProt. This approach allowed us to apply stringent cutoffs to enrich for high-confidence interactors. A full list of identified proteins and quantitative values is provided in Supplementary Table 3. For the first filter where we compared abundance of proteins labeled by PRR14L relative to no ligase control, we applied a stringent cut-off of FPI < 0.03, given that we expect that almost all the proteins identified in our no ligase control should be non-specific, using a false positive list of ER membrane proteins. For the second filter where we compared abundance of proteins labeled PRR14L relative to the nuclear spatial control, a more relaxed cut-off of FPI < 0.05 was applied. This is because a greater percentage of labeling overlap is expected when both PRR14L and the spatial control occupy the nucleus. For this cut-off, we used a false positive list of cell membrane proteins.

Acknowledgments

A.Z.L., and B.A.J. received support from the NIH Medical Scientist Training Program T32GM136577. This work was supported by Bloomberg Professorship funds to R.L. from Johns Hopkins University, a Mid-sized Grant (NRF-MSG-2023-0001) from Singapore National Research Foundation to R.L. and a Canadian Institutes of Health Research grant (FDN-167277) to M.T. We thank Angela Xiong for assistance with molecular cloning. Portions of the text were edited with the assistance of ChatGPT (OpenAI), a large language model AI tool.

522 **Declaration of Interests**

523 The authors declare no competing interests.

524 **Data and code availability**

525 Mass spectrometry and RNA-sequencing data will be deposited in publicly accessible
526 databases prior to official publication.

527

528

529

530

531

532

533

534

535

536

537

538

539

540

541 **Figure Titles and Legends**

542 **Figure 1.** NALM-6 genome-wide CRISPR/Cas9 screen identifies *PRR14L* as an
543 enhancer of NMS-P715

544 (A) Workflow of CRISPR/Cas9 screen
545 (B) (left) Rationale underlying observation of enhancer sgRNAs (center) Volcano plot
546 of CRISPR/Cas9 screen (right) Rationale underlying observation of suppressor
547 sgRNAs.
548 (C) Zoom-in on suppressor sgRNAs, with gene names highlighted, colored by gene
549 category.
550 (D) Zoom-in on enhancer sgRNAs, with gene names highlighted

551 **Figure 2.** TurboID proximity labeling of PRR14L identifies multiple cell division proteins

552 (A) Schematic of TurboID Tandem Mass Tag (TMT) mass spectrometry experiment
553 completed in HEK293T cells.
554 (B) Differences between TurboID-NLS and PRR14L-TurboID localization.
555 Representative images of hTERT RPE-1 cells transiently transfected with either
556 3xHA-TurboID-3xNLS or PRR14L-GS-3xHA-TurboID followed by 10 or 15 min
557 labeling with 50 μM biotin respectively. Images acquired on LSM980, SR-8Y
558 mode.
559 (C) Characterization of biotinylation by PRR14L-TurboID. HEK293T cells were
560 transiently transfected with either 3xHA-TurboID-3xNLS or PRR14L-GS-3xHA-
561 TurboID followed with or without incubation with 50 μM biotin for 20 min. Cell
562 lysates were used for western blot, and probed with anti-HA antibody and

563 Streptavidin Dylight 680. Untransfected (no ligase) control also included for
564 comparison.
565 (D) PRR14L proximal proteome includes cell division proteins regulated by PP2A.
566 Scatter plot of final PRR14L proximity proteome determined by mass
567 spectrometry with PRR14L itself excluded. Dots colored by GO annotation.
568 Proteins with GO annotations related to cell division have their names
569 highlighted.
570 (E) Western blot validation of PRR14L and TACC3 proximity. TurboID experiment
571 was repeated, and cell lysates were utilized for anti-TACC3 western blot.

572 **Figure 3.** Loss of *PRR14L* alters the response to anti-mitotic drugs

573 (A) Quantification of untreated mitotic duration. Beeswarm plot comparing NEBD to
574 anaphase time in HCT116 NTC and *PRR14L*$^{-/-}$ Clone A3 stably expressing H2B-
575 mNeonGreen and mCherry-CAAX measured via live cell imaging. Colors denote
576 independent experiments (n=3), small dots denote individual cells (NTC n = 48,
577 *PRR14L*$^{-/-}$ n = 48), large dots denote mean of independent experiment. p-value
578 calculated via Mann U-Whitney test using replicate averages, ns = non-
579 significant. Images acquired on Zeiss LSM 780.
580 (B) Quantification of mitotic duration in the presence of 25 nM nocodazole. Kaplan-
581 Meier curve of % of cells still remaining in mitosis in HCT116 *NTC* and *PRR14L*$^{-/-}$
582 Clone A3 stably expressing H2B-mNeonGreen and mCherry-CAAX measured
583 via live cell imaging. + marks denote censored events, where the cell still
584 remained in mitosis at the end of the movie. n = 3 independent experiments.
585 Total number of observed mitoses (NTC n = 51, PRR14L$^{-/-}$ n = 44). p-value

586 calculated via logrank test on combined data from independent experiments.
587 Images acquired on Zeiss LSM 780.

588 (C) Quantification of asymmetric chromosome partitioning in the presence of various
589 drug treatments. Combined beeswarm and bar plot comparing proportion of cells
590 undergoing asymmetric divisions between HCT116 *PRR14L*$^{+/+}$ and *PRR14L*$^{-/-}$
591 Clone A3 stably expressing H2B-mNeonGreen and mCherry-CAAX measured
592 via live cell imaging. Colors denote independent experiments (n=3), dots denote
593 mean of independent experiments with size correlated with number of mitoses
594 observed (For DMSO, *PRR14L*$^{+/+}$ n = 72, *PRR14L*$^{-/-}$ n = 77. For 1 μM NS-P715,
595 *PRR14L*$^{+/+}$ n = 68, *PRR14L*$^{-/-}$ n = 44. For 250 nM ZM447439 *PRR14L*$^{+/+}$ n = 68,
596 *PRR14L*$^{-/-}$ n = 55). p-value calculated using two-proportion Z-test using combined
597 data from independent experiments, ** = $p < 0.01$, **** = $p < 0.0001$. Images
598 acquired on Zeiss LSM 780.

599 (D) Representative images comparing live cell imaging of HCT116 *NTC* and
600 *PRR14L*$^{-/-}$ Clone A3 stably expressing H2B-mNeonGreen and mCherry-CAAX
601 with 1 μM NMS-P715 treatment. Z-max projections displayed. Frames
602 synchronized to onset of NEBD. Scale bar width = 10 μm. Images acquired on
603 Zeiss LSM 780.

604 **Figure 4.** NMS-P715 has therapeutic potential for *PRR14L* loss of function and FGFR-
605 TACC3 fusion tumors

606 (A) Flow cytometry tracking relative abundance of control and PRR14L$^{-/-}$ cells over
607 time. Cells were exposed to DMSO (1:1,000) during Days 1-3. Ribbons denote
608 standard deviation, data shown from n = 2 independent experiments.

609 (B) Flow cytometry tracking relative abundance of control and PRR14L$^{-/-}$ cells over
610 time. Cells were exposed to 1 μM NMS-P715 during Days 1-3. Ribbons denote
611 standard deviation, data shown from n = 2 independent experiments.
612 (C) Quantification of final timepoint (Day 9) of competition assay. Each dot
613 represents a single independent experiment (n = 3), and each bar represents
614 mean across independent experiments. P-value determined by one-sided
615 student's t-test, ** represents $p < 0.01$.
616 (D) Working model for PRR14L regulation of TACC3, which may potentially explain
617 *PRR14L*$^{-/-}$ phenotypes.
618 (E) Comparison of tumor cell line sensitivity between NMS-P715 and Reversine. Each point
619 represents a cancer cell line in the DepMap database. Three highlighted cell lines harbor
620 FGFR-TACC3 fusions.

621 **Figure S1.**

622 (A) Linear correlation between PRR14L-TurboID independent experiment 1 and
623 TurboID-NLS. Scatter plot displaying all proteins with >2 unique peptides
624 identified by mass spec, comparing replicate 1 against TurboID-NLS.
625 (B) Linear correlation between PRR14L-TurboID independent experiment 2 and
626 TurboID-NLS. Scatter plot displaying all proteins with >2 unique peptides
627 identified by mass spec, comparing replicate 2 against TurboID-NLS.
628 (C) Linear correlation between PRR14L-TurboID independent experiment 1 and
629 independent experiment 2. Scatter plot displaying all proteins with >2 unique
630 peptides identified by mass spec, comparing replicate 2 against replicate 1.

631 (D) Determination of filter 1 cut-off for independent experiment 1. False positive
632 protein list used was ER membrane proteins from Uniprot. False positive
633 identification plotted against log_2 ratio comparing independent experiment 1 and
634 no ligase control. Log_2 cut-off determined at a FPI = 0.03 (3% of false positive
635 proteins have log_2 ratios higher than the cut-off of 0.592).
636 (E) Determination of filter 1 cut-off for independent experiment 2. False positive
637 protein list used was ER membrane proteins from Uniprot. False positive
638 identification plotted against log_2 ratio comparing independent experiment 2 and
639 no ligase control. Log_2 cut-off determined at a FPI = 0.03 (3% of false positive
640 proteins have log_2 ratios higher than the cut-off of 0.804).
641 (F) Determination of filter 2 cut-off for independent experiment 1. False positive
642 protein list used was cell membrane proteins from Uniprot. False positive
643 identification plotted against log_2 ratio comparing independent experiment 1 and
644 spatial control. Log_2 cut-off determined at a FPI = 0.05 (5% of false positive
645 proteins have log_2 ratios higher than the cut-off of 0.335).
646 (G) Determination of filter 2 cut-off for independent experiment 2. False positive
647 protein list used was cell membrane proteins from Uniprot. False positive
648 identification plotted against log_2 ratio comparing independent experiment 2 and
649 spatial control. Log_2 cut-off determined at a FPI = 0.05 (5% of false positive
650 proteins have log_2 ratios higher than the cut-off of 0.603).
651 (H) Scatter plot displaying filter one and two for independent experiment 1.
652 (I) Scatter plot displaying filter one and two for independent experiment 2.

653 (J) Final PRR14L proximity proteome list. Most enriched protein is clearly PRR14L
654 itself.
655 (K) Final PRR14L proximity proteome list with PRR14L excluded and phosphatase
656 regulatory subunit genes highlighted, via GO annotations containing
657 "dephosphorylation."
658 (L) Final PRR14L proximity proteome list with PRR14L excluded and protein quality
659 control genes highlighted, via GO annotations containing "proteasome,"
660 "ubiquitin," and/or "protein folding."
661 (M) Final PRR14L proximity proteome list with PRR14L excluded and nuclear import
662 genes highlighted, via GO annotation containing "import into nucleus."
663 (N) Final PRR14L proximity proteome list with PRR14L excluded and mitochondrial
664 genes highlighted, via GO annotation containing "mitoch."

665

666 **Figure S2.**

667 (A) Genotyping validation of *PRR14L*$^{-/-}$ monoclonal HCT116 cells. Sanger
668 sequencing traces aligned to genomic sequence from genome assembly hg38.
669 (B) qPCR quantification of PRR14L mRNA in *PRR14L*$^{-/-}$ HCT116 cells. mRNA fold
670 change calculated via ddCt method, using *ACTB* as a control. Each dot
671 represents a single independent experiment (n = 3), and each bar represents
672 mean across independent experiments. P-value determined by one-sided
673 student's t-test, ** represents $p < 0.01$.
674 (C) Gene Set Enrichment Analysis (GSEA) of MSigDB Hallmark pathways. RNA-seq
675 data from HCT116 *PRR14L*$^{-/-}$ (KO) and NTC cells were analyzed. Genes were

676 ranked by the Wald statistic derived from DESeq2. The dot plot shows the
677 significantly enriched pathways (FDR < 0.05), faceted by activation (positive
678 Normalized Enrichment Score, NES) or suppression (negative NES) in *PRR14L*$^{-/-}$
679 cells. Dot size corresponds to the number of genes in the leading edge, and color
680 indicates the FDR-adjusted p-value.

681 (D) Differential pathway activity inference using PROGENy. VST-normalized
682 expression data was used as input to estimate the activity of 14 major signaling
683 pathways based on the expression of pathway footprint genes. The bar plot
684 displays the change in activity score (KO - NTC). Bars are colored based on
685 significance and direction of change. FDR values are indicated next to the
686 corresponding bars.

687 **Figure S3.**

688 (A) Metaphase spread counts (untreated). Histogram comparing chromosome
689 number between HCT116 NTC and HCT116 PRR14L$^{-/-}$ Clone A3. Bin width
690 displayed = 1. Data combined from n = 3 independent experiments. Total number
691 of spreads counted (NTC n = 101, PRR14L$^{-/-}$ n = 96). p-value calculated via two-
692 sided student's t-test using replicate averages.

693 (B) Metaphase spread counts (1 μM NMS-P715 treatment). Histogram comparing
694 chromosome number between HCT116 NTC and HCT116 PRR14L$^{-/-}$ Clone A3.
695 Bin width displayed = 3. Data from n = 1 independent experiment. Total number
696 of spreads counted (NTC n = 42, PRR14L$^{-/-}$ n = 42).

697 (C) Representative images comparing live cell imaging of HCT116 NTC and
698 PRR14L$^{-/-}$ Clone A3 stably expressing H2B-mNeonGreen and mCherry-CAAX

699 with 250 nM ZM 447439 treatment. Z-max projections displayed. Frames
700 synchronized to onset of NEBD. Scale bar width = 10 μm. Images acquired on
701 LSM780.
702 (D) Quantification of final timepoint (Day 9) of competition assay. Each dot
703 represents a single independent experiment (n = 2 or 1), and each bar
704 represents mean across independent experiments. DMSO values are the same
705 as independent experiments 1 and 2 from Fig. 4C.

706 **Supplementary Table 3.** Full list of proteins identified and quantified in the PRR14L
707 TurboID-MS experiment.

708

709 **References**

710 Ando, R, Shimozono, S, Ago, H, Takagi, M, Sugiyama, M, Kurokawa, H, Hirano, M,
711 Niino, Y, Ueno, G, Ishidate, F, *et al.* (2024). StayGold variants for molecular fusion and
712 membrane-targeting applications. Nat Methods 21, 648–656.

713 Baker, DJ, Jeganathan, KB, Cameron, JD, Thompson, M, Juneja, S, Kopecka, A,
714 Kumar, R, Jenkins, RB, De Groen, PC, Roche, P, *et al.* (2004). BubR1 insufficiency
715 causes early onset of aging-associated phenotypes and infertility in mice. Nat Genet 36,
716 744–749.

717 Baker, TM, Waise, S, Tarabichi, M, and Van Loo, P (2024). Aneuploidy and complex
718 genomic rearrangements in cancer evolution. Nat Cancer 5, 228–239.

719 Bakhoum, SF, and Landau, DA (2017). Chromosomal instability as a driver of tumor
720 heterogeneity and evolution. Cold Spring Harb Perspect Med 7.

721 Bakhoum, SF, Ngo, B, Laughney, AM, Cavallo, JA, Murphy, CJ, Ly, P, Shah, P, Sriram,
722 RK, Watkins, TBK, Taunk, NK, *et al.* (2018). Chromosomal instability drives metastasis
723 through a cytosolic DNA response. Nature 553, 467–472.

724 Bertomeu, T, Coulombe-Huntington, J, Chatr-aryamontri, A, Bourdages, KG, Coyaud, E,
725 Raught, B, Xia, Y, and Tyers, M (2018). A High-Resolution Genome-Wide CRISPR/Cas9
726 Viability Screen Reveals Structural Features and Contextual Diversity of the Human
727 Cell-Essential Proteome. Mol Cell Biol 38, 1–24.

728 Booth, DG, Hood, FE, Prior, IA, and Royle, SJ (2011). A TACC3/ch-TOG/clathrin
729 complex stabilises kinetochore fibres by inter-microtubule bridging. EMBO Journal 30,
730 906–919.

731 Branon, TC, Bosch, JA, Sanchez, AD, Udeshi, ND, Svinkina, T, Carr, SA, Feldman, JL,
732 Perrimon, N, and Ting, AY (2018). Efficient proximity labeling in living cells and
733 organisms with TurboID. Nat Biotechnol 36, 880–898.

734 Capelletti, M, Dodge, ME, Ercan, D, Hammerman, PS, Park, S Il, Kim, J, Sasaki, H,
735 Jablons, DM, Lipson, D, Young, L, *et al.* (2014). Identification of recurrent FGFR3-
736 TACC3 fusion oncogenes from lung adenocarcinoma. Clinical Cancer Research 20,
737 6551–6558.

738 Carneiro, BA, Elvin, JA, Kamath, SD, Ali, SM, Paintal, AS, Restrepo, A, Berry, E, Giles,
739 FJ, and Johnson, ML (2015). FGFR3-TACC3: A novel gene fusion in cervical cancer.
740 Gynecol Oncol Rep 13, 53–56.

741 Chase, A, Pellagatti, A, Singh, S, Score, J, Tapper, WJ, Lin, F, Hoade, Y, Bryant, C,
742 Trim, N, Yip, BH, *et al.* (2019). PRR14L mutations are associated with chromosome 22
743 acquired uniparental disomy, age-related clonal hematopoiesis and myeloid neoplasia.
744 Leukemia 33, 1184–1194.

745 Chase, A, Tarragona, GC, Lin, F, Yapp, S, Score, J, Bryant, C, and Cross, NCP (2023).
746 Identification of B56 α , B56 γ and BAP1 as PRR14L binding partners. 1–15.

747 Cho, KF, Branon, TC, Udeshi, ND, Myers, SA, Carr, SA, and Ting, AY (2020). Proximity
748 labeling in mammalian cells with TurboID and split-TurboID. Nat Protoc 15, 3971–3999.

749 Colombo, R, Caldarelli, M, Mennecozzi, M, Giorgini, ML, Sola, F, Cappella, P, Perrera,
750 C, Re Depaolini, S, Rusconi, L, Cucchi, U, *et al.* (2010). Targeting the mitotic checkpoint
751 for cancer therapy with NMS-P715, an inhibitor of MPS1 kinase. Cancer Res 70,
752 10255–10264.

753 Conant, D, Hsiau, T, Rossi, N, Oki, J, Maures, T, Waite, K, Yang, J, Joshi, S, Kelso, R,
754 Holden, K, *et al.* (2022). Inference of CRISPR Edits from Sanger Trace Data. CRISPR
755 Journal 5, 123–130.

756 Dobles, M, Liberal, V, Scott, ML, Benezra, R, and Sorger, PK (2000). Chromosome
757 Missegregation and Apoptosis in Mice Lacking the Mitotic Checkpoint Protein Mad2, Li
758 and Nicklas.

759 Gibson, DG, Young, L, Chuang, R-Y, Venter, JC, Hutchison, CA, and Smith, HO (2009).
760 Enzymatic assembly of DNA molecules up to several hundred kilobases. Nat Methods
761 6, 343–345.

762 Gill, KP, and Denham, M (2020). Optimized Transgene Delivery Using Third-Generation
763 Lentiviruses. Curr Protoc Mol Biol 133.

764 Gordon, DJ, Resio, B, and Pellman, D (2012). Causes and consequences of aneuploidy
765 in cancer. Nat Rev Genet 13, 189–203.

766 Hewitt, L, Tighe, A, Santaguida, S, White, AM, Jones, CD, Musacchio, A, Green, S, and
767 Taylor, SS (2010). Sustained Mps1 activity is required in mitosis to recruit O-Mad2 to the
768 Mad1-C-Mad2 core complex. Journal of Cell Biology 190, 25–34.

769 Johnson, BA, Liu, AZ, Bi, T, Dong, Y, Li, T, Zhou, D, Narkar, A, Wu, Y, Sun, SX, Larman,
770 TC, *et al.* (2024). Simple aneuploidy evades p53 surveillance and promotes niche
771 factor-independent growth in human intestinal organoids. Mol Biol Cell.

772 Katoh, Y, Michisaka, S, Nozaki, S, Funabashi, T, Hirano, T, Takei, R, and Nakayama, K
773 (2017). Practical method for targeted disruption of cilia-related genes by using
774 CRISPR/Cas9-mediated, homology-independent knock-in system. Mol Biol Cell 28,
775 898–906.

776 Koh, S-B, Mascalchi, P, Rodriguez, E, Lin, Y, Jodrell, DI, Richards, FM, and Lyons, SK
777 (2017). A quantitative FastFUCCI assay defines cell cycle dynamics at a single-cell
778 level. J Cell Sci 130, 512–520.

779 Lara-Gonzalez, P, Pines, J, and Desai, A (2021). Spindle assembly checkpoint
780 activation and silencing at kinetochores. Semin Cell Dev Biol 117, 86–98.

781 Lin, CH, Hu, CK, and Shih, HM (2010). Clathrin heavy chain mediates TACC3 targeting
782 to mitotic spindles to ensure spindle stability. Journal of Cell Biology 189, 1097–1105.

783 Narkar, A, Johnson, BA, Bharne, P, Zhu, J, Padmanaban, V, Biswas, D, Fraser, A,
784 Iglesias, PA, Ewald, AJ, and Li, R (2021). On the role of p53 in the cellular response to
785 aneuploidy. Cell Rep 34, 108892.

786 Normandin, K, Coulombe-Huntington, J, St-Denis, C, Bernard, A, Bourouh, M,
787 Bertomeu, T, Tyers, M, and Archambault, V (2023). Genetic enhancers of partial PLK1
788 inhibition reveal hypersensitivity to kinetochore perturbations. PLoS Genet 19.

789 Pemble, H, Kumar, P, van Haren, J, and Wittmann, T (2017). GSK3-mediated CLASP2
790 phosphorylation modulates kinetochore dynamics. J Cell Sci 130, 1404–1412.

791 Replogle, JM, Zhou, W, Amaro, AE, Mcfarland, JM, Villalobos-Ortiz, M, Ryan, J, Letai, A,
792 Yilmaz, O, Sheltzer, J, Lippard, SJ, *et al.* (2020). Aneuploidy increases resistance to
793 chemotherapeutics by antagonizing cell division.

794 Sanjana, NE, Shalem, O, and Zhang, F (2014). Improved vectors and genome-wide
795 libraries for CRISPR screening. Nat Methods 11, 783–784.

Sansregret, L, Patterson, JO, Dewhurst, S, López-García, C, Koch, A, McGranahan, N, Chao, WCH, Barry, DJ, Rowan, A, Instrell, R, *et al.* (2017). APC/C dysfunction limits excessive cancer chromosomal instability. Cancer Discov 7, 218–233.

Santaguida, S, Tighe, A, D'Alise, AM, Taylor, SS, and Musacchio, A (2010). Dissecting the role of MPS1 in chromosome biorientation and the spindle checkpoint through the small molecule inhibitor reversine. Journal of Cell Biology 190, 73–87.

Schneider, CA, Rasband, WS, and Eliceiri, KW (2012). NIH Image to ImageJ: 25 years of image analysis. Nat Methods 9, 671–675.

Schvartzman, JM, Sotillo, R, and Benezra, R (2010). Mitotic chromosomal instability and cancer: Mouse modelling of the human disease. Nat Rev Cancer 10, 102–115.

Singh, D, Chan, JM, Zoppoli, P, Niola, F, Sullivan, R, Castano, A, Liu, EM, Reichel, J, Porrati, P, Pellegatta, S, *et al.* (2012). Transforming Fusions of FGFR and TACC Genes in Human Glioblastoma. Science (1979) 337, 1231–1235.

Smela, MDP, Kramme, CC, Fortuna, PRJ, Adams, JL, Su, R, Dong, E, Kobayashi, M, Brixi, G, Kavirayuni, VS, Tysinger, E, *et al.* (2023). Directed differentiation of human iPSCs to functional ovarian granulosa-like cells via transcription factor overexpression. Elife 12.

Still, IH, Vince, P, and Cowell, JK (1999). The Third Member of the Transforming Acidic Coiled Coil-Containing Gene Family, TACC3, Maps in 4p16, Close to Translocation Breakpoints in Multiple Myeloma, and Is Upregulated in Various Cancer Cell Lines.

Thompson, SL, and Compton, DA (2008). Examining the link between chromosomal instability and aneuploidy in human cells. Journal of Cell Biology 180, 665–672.

Vallardi, G, Allan, LA, Crozier, L, and Saurin, AT (2019). Division of labour between pp2a-b56 isoforms at the centromere and kinetochore. Elife 8, 1–25.

Wickham, H (2016). ggplot2 Elegant Graphics for Data Analysis Second Edition, Houston.

Wong, S-S, Monteiro, JM, Chang, C-C, Peng, M, Mohamed, N, Steinacker, TL, Xiao, B, Saurya, S, Wainman, A, and Raff, JW (2025). Centrioles generate two scaffolds with distinct biophysical properties to build mitotic centrosomes. Sci Adv.

Figure 1

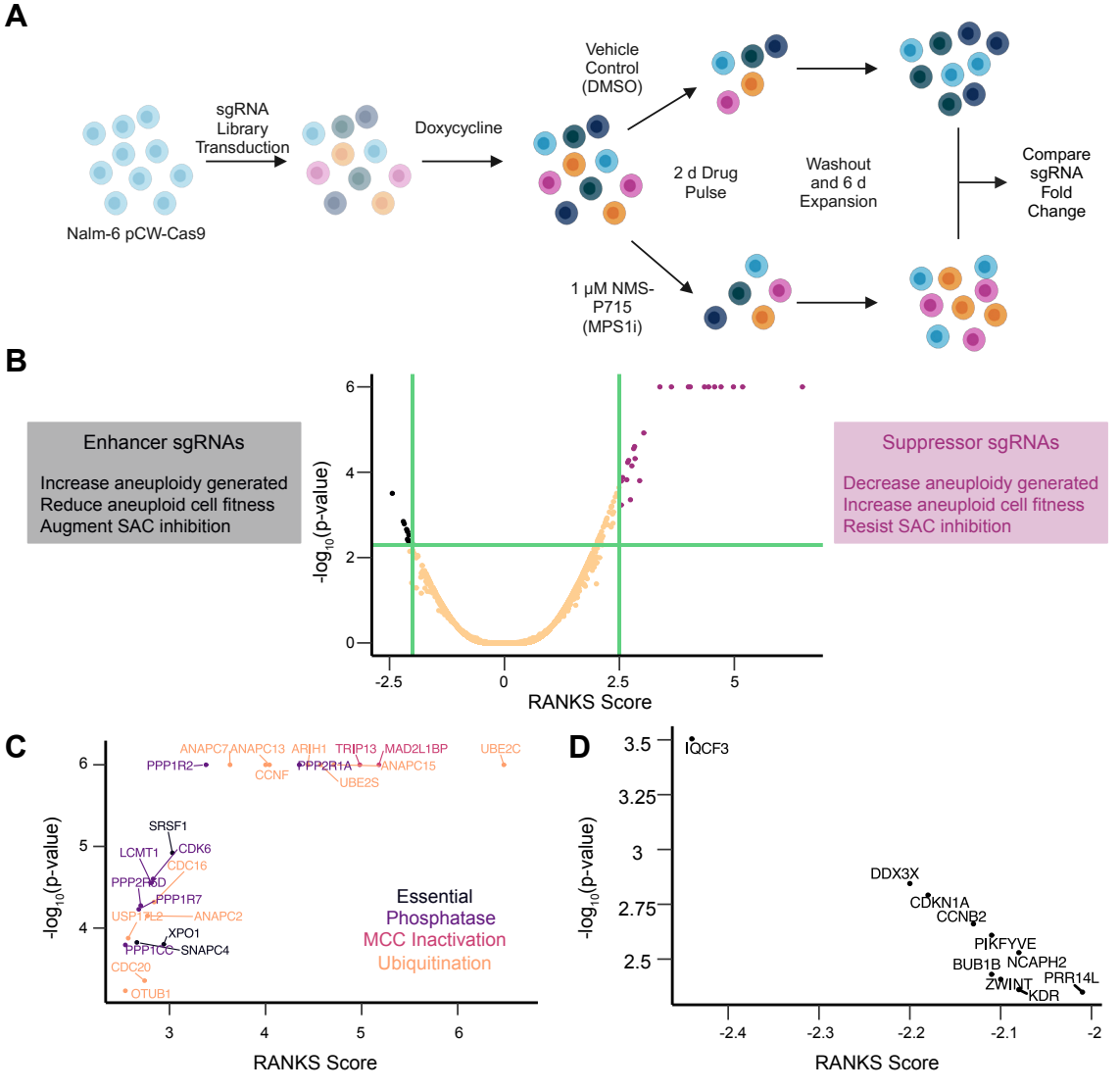
A
Nalm-6 pCW-Cas9
sgRNA Library Transduction
Doxycycline
Vehicle Control (DMSO)
2 d Drug Pulse
1 μM NMS-P715 (MPS1i)
Washout and 6 d Expansion
Compare sgRNA Fold Change
B
Enhancer sgRNAs
Increase aneuploidy generated
Reduce aneuploid cell fitness
Augment SAC inhibition
Suppressor sgRNAs
Decrease aneuploidy generated
Increase aneuploid cell fitness
Resist SAC inhibition
-log10(p-value)
RANKS Score
C
PPP1R2
ANAPC7
ANAPC13
ARIH1
TRIP13
MAD2L1BP
UBE2C
CCNF
PPP2R1A
ANAPC15
UBE2S
SRSF1
LCMT1
CDK6
CDC16
PPP2R6D
PPP1R7
USP17L2
ANAPC2
XPO1
PPP1CC
SNAPC4
CDC20
OTUB1
Essential
Phosphatase
MCC Inactivation
Ubiquitination
-log10(p-value)
RANKS Score
D
IQCF3
DDX3X
CDKN1A
CCNB2
PIKFYVE
BUB1B
NCAPH2
ZWINT
PRR14L
KDR
-log10(p-value)
RANKS Score

Figure 2

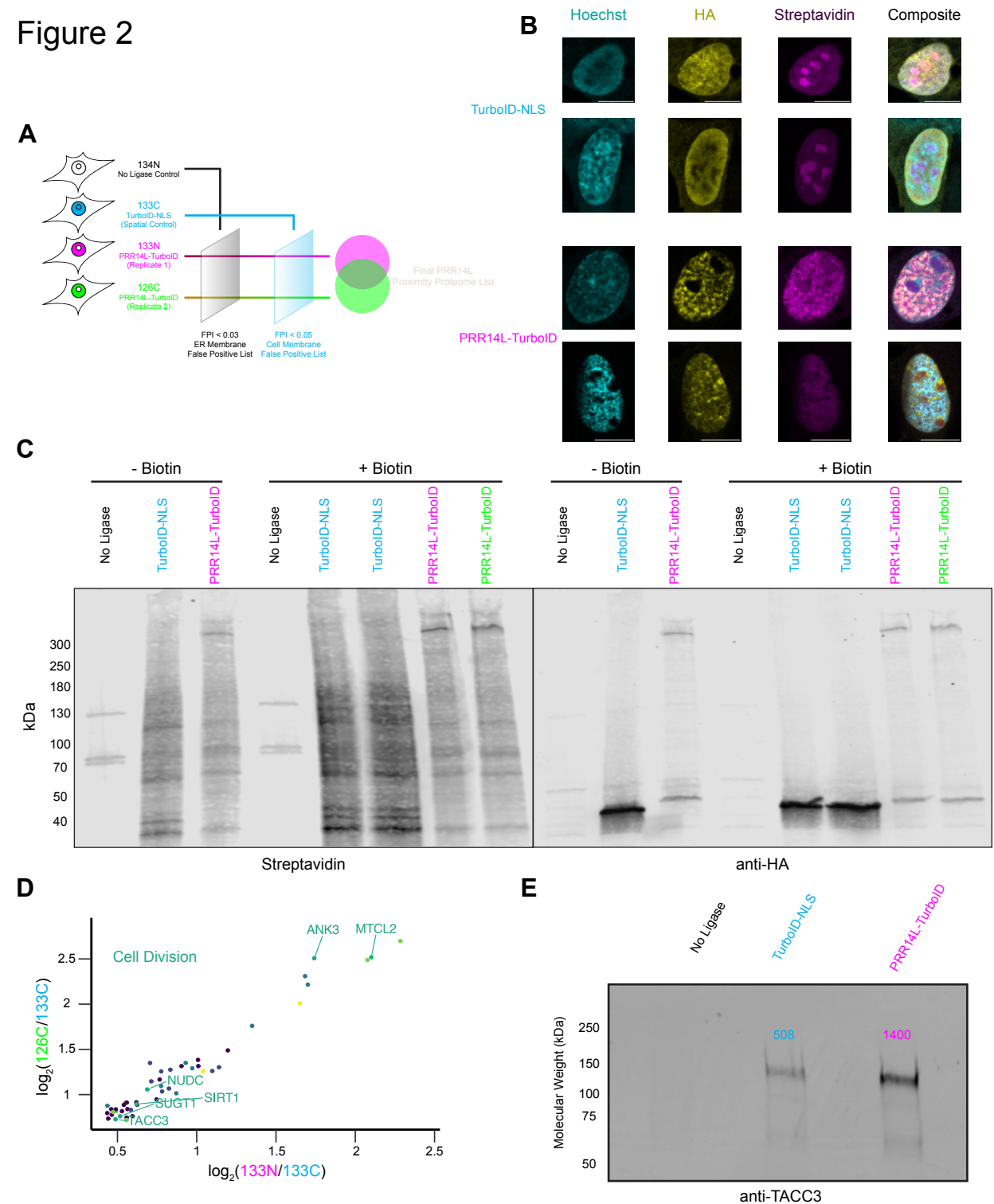
A
134N
No Ligase Control
133C
TurboID-NLS
(Spatial Control)
133N
PRR14L-TurboID
(Replicate 1)
126C
PRR14L-TurboID
(Replicate 2)
FPI < 0.03
ER Membrane
False Positive List
FPI < 0.05
Cell Membrane
False Positive List
Final PRR14L
Proximity Proteome List
B
Hoechst
HA
Streptavidin
Composite
TurboID-NLS
PRR14L-TurboID
C
- Biotin
+ Biotin
- Biotin
+ Biotin
No Ligase
TurboID-NLS
PRR14L-TurboID
kDa
300
250
180
130
100
70
50
40
Streptavidin
anti-HA
D
Cell Division
ANK3
MTCL2
NUDC
SIRT1
SUGT1
TACC3
log2(126C/133C)
log2(133N/133C)
E
No Ligase
TurboID-NLS
PRR14L-TurboID
Molecular Weight (kDa)
250
150
100
75
50
508
1400
anti-TACC3

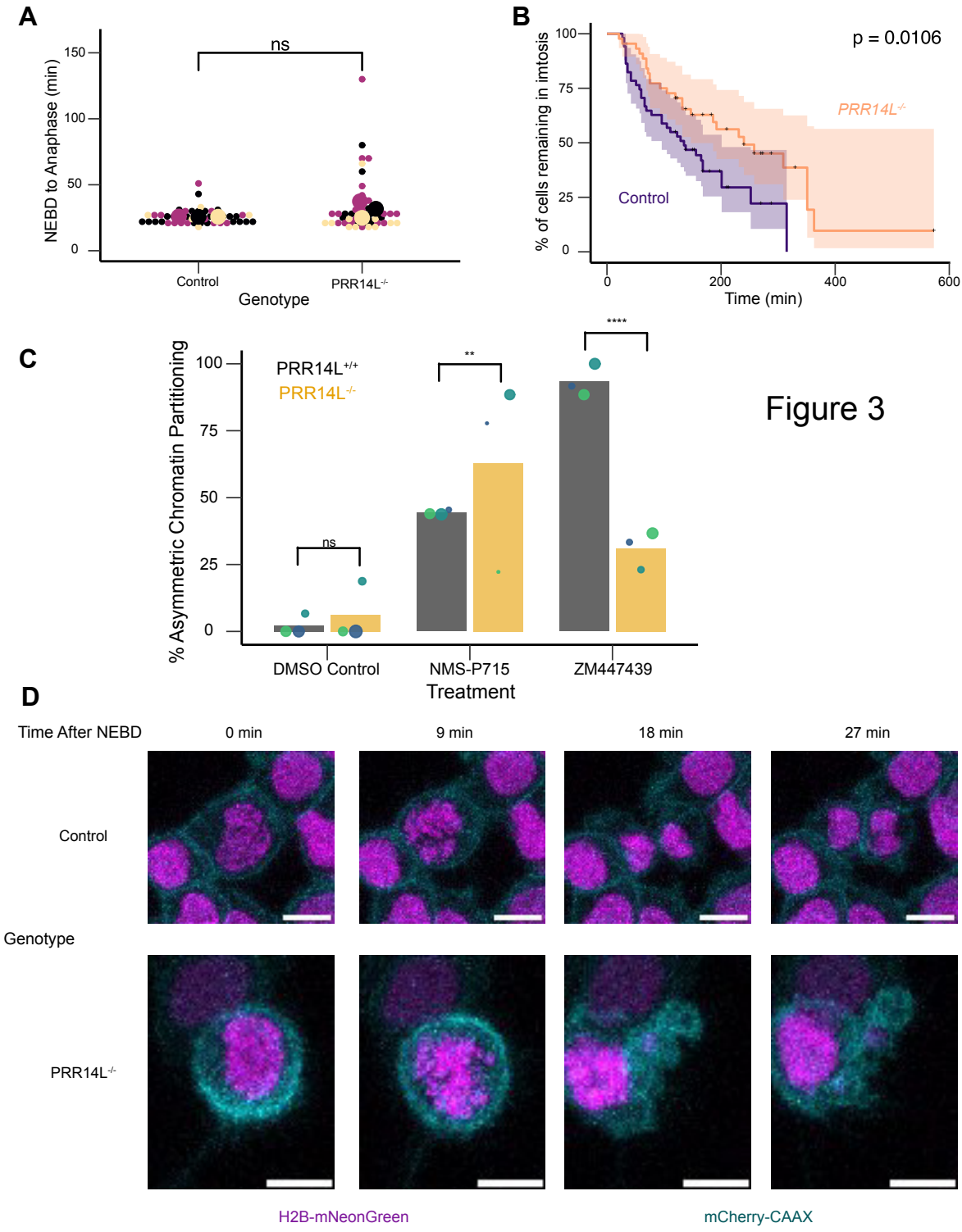
A
NEBD to Anaphase (min)
150
100
50
0
ns
Control
PRR14L-/-
Genotype
B
% of cells remaining in imtosis
100
75
50
25
0
p = 0.0106
PRR14L-/-
Control
0
200
400
600
Time (min)
C
% Asymmetric Chromatin Partitioning
100
75
50
25
0
PRR14L+/+
PRR14L-/-
ns
**
****
DMSO Control
NMS-P715
ZM447439
Treatment
Figure 3
D
Time After NEBD
0 min
9 min
18 min
27 min
Control
Genotype
PRR14L-/-
H2B-mNeonGreen
mCherry-CAAX

Figure 4

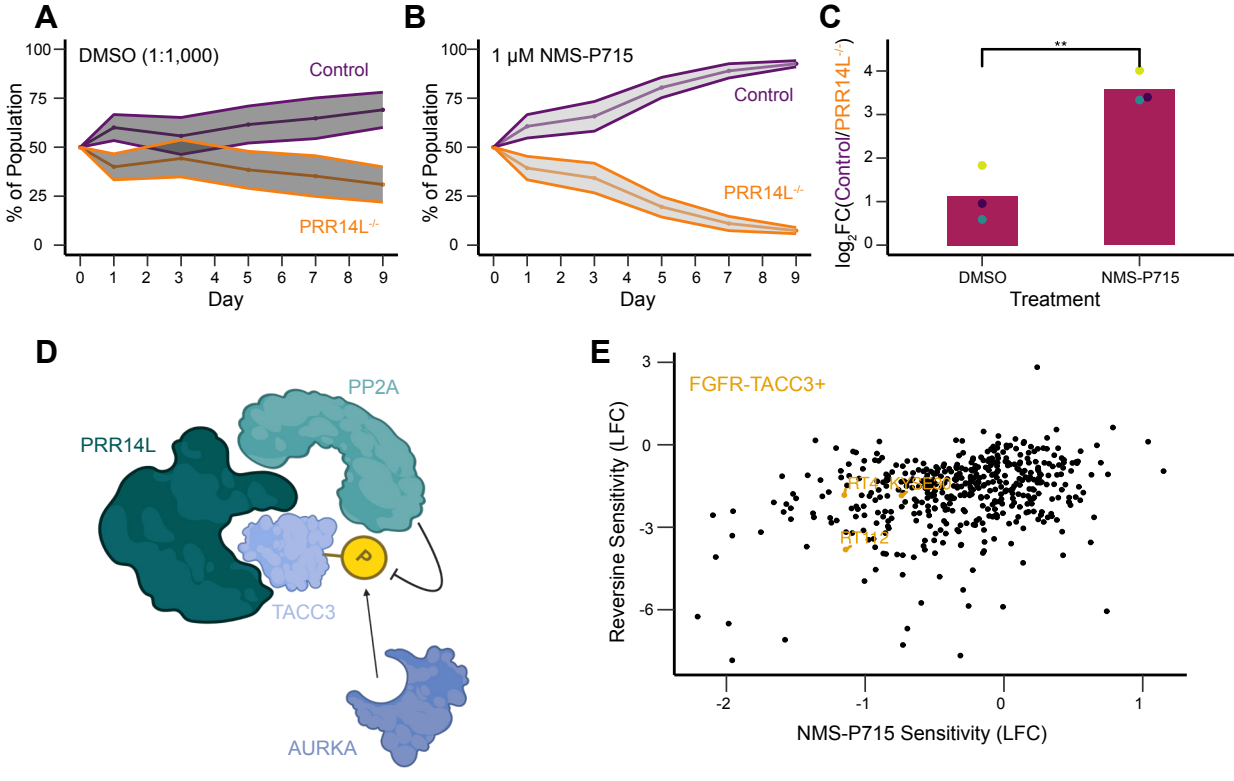
A
DMSO (1:1,000)
Control
PRR14L-/-
% of Population
Day
B
1 μM NMS-P715
Control
PRR14L-/-
% of Population
Day
C
**
log2FC(Control/PRR14L-/-)
DMSO
NMS-P715
Treatment
D
PP2A
PRR14L
TACC3
P
AURKA
E
FGFR-TACC3+
PRR14L
Reversine Sensitivity (LFC)
NMS-P715 Sensitivity (LFC)